Design and Preliminary Results of a Reaction Force Series Elastic Actuator for Bionic Knee and Ankle Prostheses

Matthew E. Carney,[1] *Member, IEEE*, Tony Shu,[1] Roman Stolyarov,[1] Jean-François Duval,[2] Hugh Herr,[1]

***Abstract*—We present an actuator designed for untethered, lower-extremity powered-prostheses that replicates biological kinetic and kinematic function of both human knees and ankles. An electric energy optimal hardware specification is defined by kinematically clamping walking gait data to the dynamic model of a series elastic actuator (SEA) and searching for motor, reduction ratio, and spring. The actuator is shown to achieve the required torque, angle, and velocity requirements for nominal walking conditions on level ground as well as varied terrain. The performance of the actuator is demonstrated on benchtop and as worn by a human subject with unilateral below knee amputation. The resulting design is a moment-coupled cantilever-beam reaction-force SEA (MC-RFSEA) that has a nominal torque rating of 85Nm, repeated peak torque of 175Nm, 105^{o}range of motion, and a hardware mass of 1.6kg. Preliminary results from level-ground walking with the actuator tested in an ankle configuration show an electric cost of transport of 0.053J/kg when walking at 1.5m/s.**

***Index Terms*—robotics, prostheses, actuator, ankle, knee.**

I. Introduction

A little more than a decade after the first powered ankle prosthesis, research in lower-extremity rehabilitation robotics remains limited by a lack of commercial and academic hardware platforms capable of producing biologically relevant dynamics. The commercial off the shelf powered ankle and knee systems are not able to provide biologically accurate kinetics with kinematics, nor do they enable access to the underlying control systems [1], [2]. To improve upon the commercial options, a growing handful of academic research groups around the world have been building individualized platforms for study. Most of these academic platforms have remained within their own labs requiring each lab to build its own hardware. This paper describes the mechanical design of an autonomous, untethered, wearable, series elastic actuator topology that aims to achieve biologically relevant kinetics and kinematics of both a human knee and ankle, while reducing hardware complexity and remaining within the mass bounds of human equivalent leg segments.

Manuscript received Month, Year.

Financial support: this work was supported in part by the MIT Media Lab Consortia, the U.S. Army Medical Research and Materiel Command (W81XWH-14-C-0111) and the Defense Advanced Research Projects Agency (W911NF-17-2-0043).

[1]MIT Center for Extreme Bionics and MIT Media Lab - Biomechatronics Group, Massachusetts Institute of Technology, Cambridge, MA 02139 USA. e-mail: mcarney@media.mit.edu.

[2]Dephy, Inc., Maynard, MA 01754 USA.

The first powered ankle, published by Au, Weber, Herr, used a series elastic actuator (SEA) [3] configured with a parallel spring to improve torque bandwidth in the transition from controlled dorsiflexion to powered-push-off. Au *et al.* showed that the actuator's ability to contribute energy during powered push-off improved the metabolic cost of walking [4]. Since then numerous actuators have been designed following a similar topology [5]–[9]. Many of these designs have focused around flat, level-ground walking, where primary kinetic behavior occurs as a large power maneuver during powered plantar flexion. Commercial devices such as the BiOM/EmPower [10] even limit joint range to zero dorsiflexion in order to reduce electric energy expenditure. To improve control bandwidth and electrical energetics parallel springs are frequently used, at a cost of range of motion and terrain adaptability.

Though well designed for flat ground, and self-selected walking speed, these powered prostheses quickly hit kinematic limits at higher walking velocities and varied terrain. At higher walking speed, stride length and joint angle excursion increase[11]. Mean data from nine subjects walking at 0.75m/s to 2.0m/s shows ankle dorsiflexion angle increases from 8.3 to 19.3 degrees. These range of motion limitations are compounded when encountering sloped surfaces or stairs. During stair descent a 21 degree mean dorsiflexion angle is reached during stance, and up to 40 degrees mean plantarflexion angle in swing phase [12]. To demonstrate the difference between laboratory experiments and real-world consider: the ADA compliant wheelchair ramp slope specification declares a maximum 7.1 degree inclination. Fast walking up such a ramp would limit proper kinematic function in all the ankles described except for the Vanderbilt legs.

Powered knee actuators tend to be large and disregard clearance height that would allow for separate powered ankles; combined knee and ankle powered prostheses can enable coordinated motion at the knee and ankle allowing for more complex and bio-mimmetic control techniques. However, they are frequently designed to a single specific height, restricting usability to a very limited patient group. Many also forgo full torque control throughout the entire gait cycle, and instead provide closed-loop control only during specific phases. The commercially available Össur Power Knee weighs 3.1kg, has a clearance height of 270mm, and from the datasheet appears to only support limited position control in specific states, rather than provide full torque controlled impedance modes [2]. The Vanderbilt Leg 2.0 knee is a 2.7kg mass with a 85Nm max

load, and no power rating. The Vanderbilt Leg 3.0 appears to have a fixed height of 452mm limiting its use by smaller patients who are more well matched to the torque capability of the system [13]. The University of Utah *Romeo* knee sports an actively variable transmission (AVT) that can be adjusted when the system is unloaded, but is not not actively powered [14]; it has a mass of 1.7kg and a 290mm build height. The MIT Clutched Series Elastic Actuator (*CSEA*) was designed to conserve electric energy with a brake on the motor shaft, and asymmetric flexion and extension springs; it has a 2.7kg mass and 280mm clearance [15]. The MIT Agonist-antagonist knee actuator that uses two series elastic actuators acting against each other to set the joint stiffness has substantial torque capability at 130Nm, but mass of 3kg and build height of 330mm [16]. The AMPRO 3 is a fixed height combined knee and ankle prosthesis that makes use of harmonic drives, and spiral series elastic springs for torque control; the system mass is 5.95kg and peak 123Nm torque at the ankle [17].

In this study we present the mechanical design of TF8[1]. The design is based on kinematically clamped simulation and optimization methods described in our paper examining electric energetics in prostheses [18]. In that paper we propose the possibility of a single actuator topology that achieves biologically relevant knee and ankle motions and forces, while maintaining an electric energy cost of transport that could be serviced by a reasonably sized battery for a days worth of walking. The hypothesis we propose to test here is that it is possible to design an electrically efficient, multi-purpose actuator capable of achieving the knee and ankle kinetics and kinematics required for walking, ramp, stair ascents/descents, and possibly fall recovery, while remaining within the mass constraints of equivalent leg segments, all while also reducing cost and maintenance complexity for laboratory researchers. The first section of this manuscript explains the specifics of the chosen architecture and mechatronic system. We then present preliminary results of the actuator tested on benchtop, and worn by a human subject with unilateral below knee amputation. Finally, we end offering some guidance for future efforts.

Fig. 1. The TF8 Actuator is designed to operate as either a knee or ankle powered prosthesis. Shown here are two TF8 actuators stacked into a combined powered knee-ankle prosthesis.

II. Mechanical Design

A. Design Specification

The design specification for range of motion, torque, power, and system bandwidth, are gathered from analysis of 1005 unique, mass-normalized, gait cycles of walking data from nine able-bodied subjects [19]. We set the performance target based on a 90kg user walking at a near jogging pace of 2.0m/s. Range of motion of the joints is increased beyond walking to accommodate varied terrain such as ramps and stairs [12], [20]. The velocity requirements are set for fast walking. A reach design criteria would increase knee velocity capability to 9.5 rad/s for trip recovery [21]. The allowable mass is based on the mass of a human calf and foot segment [22], [23]. For maximum ankle mass we assume the mass of a foot and one third of the calf mass, or 2.9% of body mass. Table I summarizes the design targets and the resulting performance of the actuator.

[1]The TF8 name comes from being the eighth major design iteration of a powered transfemoral prosthesis.

B. System Design

To find the main design parameters of the mechatronic design (motor, transmission ratio and series stiffness) we apply a gradient descent optimization with non-linear constraints to a model of mechanical and electrical systems dynamics. The process is similar to methods in [24]–[26], where joint mean torque, velocity and angle trajectories aggregated from [19] are mass normalized, scaled and clamped to the dynamic equations for a series elastic actuator. The performance requirements of the motor are then evaluated by the optimization procedure. Constraints include defined maximum allowable motor phase voltage and current as well as torque and velocity limits of

TABLE I
ACTUATOR DESIGN SPECIFICATION

2m/s	Ankle	Knee	Target	Result	Units
Range of Motion[1]	21-0-40	72	45-0-65	35-0-75*	*Deg*
Velocity	6.0	8.6	9.5	6.8**	*rad/s*
Max Torque[2]	160	118	175	175	*Nm*
Max Power	552	313	550	350**	*W*
Bandwidth Magnitude	82	73	82	82	*Nm*
Bandwidth Frequency	4.8	6.0	6.0	6.2	*Hz*
Segment Mass	2.6	2.6	2.0	1.6	*kg*

[1] Range of motion as shown: *dorsiflexion - neutral - plantar flexion*.
[2] Fatigue limit for repeated torques.
* The knee configuration is biased to make use of a total 110 degree ROM.
** Limited by current instantiation of power electronics.

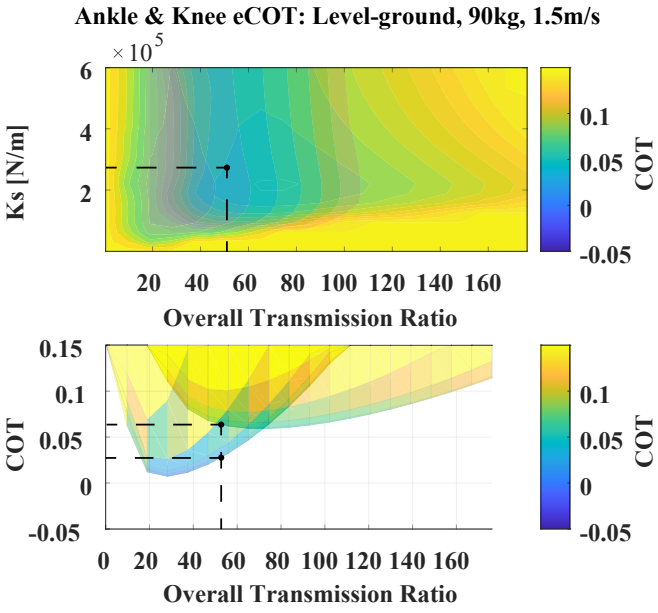

Fig. 2. Overlaying the knee level-ground energetic map with that from the ankle there is a compromise region where both systems can operate with the same hardware configuration. The dotted lines show the as built overall gear ratio and expected eCOT performance, evaluated with a 90kg person walking at 1.5m/s.

the motors. The procedure steps through a database of motors to evaluate optimal configurations for each motor.

In our paper [18] we demonstrate this optimization procedure and define a search objective to minimize the electric Cost of Transport (eCOT) for a gait cycle. The results of this simulation is the driving force for the design here presented. The eCOT overlays in Fig. 2 define a design point that satisfies both knee and ankle kinetics and kinematics while requiring acceptable electric energy to perform 3000 steps/charge. This performance is achieved, in simulation, at least, by storing nearly 14J of energy in an elastic element.

In order to package such a high energy-density spring we narrow the design to use a ball-screw and linkage drive train. We then implement secondary tiered optimization searches to identify energy optimal joint linkage geometry and a mass optimized spring that can accommodate operating as both a knee and ankle.

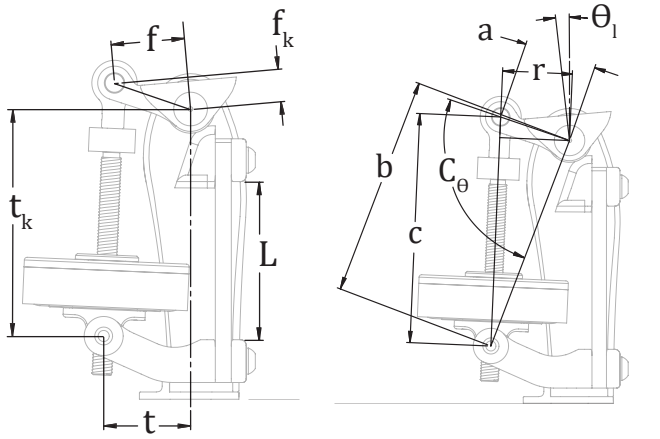

(a) (b)

Fig. 3. (a) The actuator geometry parameters t, t_k, f, f_k, L are found through optimization. The objective was finding moment arm geometry with the most efficient configuration of the power stroke as specified by the load trajectory and actuator dynamics. (b) Parameters used for calculating instantaneous moment-arm length for control.

1) Drivetrain: Joint torque is generated by a linear actuator that acts on a moment arm about the joint axis. The linear actuator is composed of a ball-screw with ball-nut integrated directly into the motor rotor. The rotation of the screw is constrained by a push-rod end affixed to one end that pivots around an orthogonal axis located a projected distance from joint axis. To tune the linkage geometry to match the power-stroke of an ankle gait cycle, we used a gradient descent search and set the search objective to minimize eCOT. The linkage parameters we searched for f, f_k, t, t_k are defined in Fig. 3.

The moment arm across which the screws applies a torque about the joint is defined as:

$$C_\theta = \pi - \theta_l - (T + F) \tag{1}$$

$$c = \sqrt{a^2 + b^2 - 2 \cdot a \cdot b \cdot cos(C_\theta)} \tag{2}$$

$$r = b \cdot \sqrt{1 - \left(\frac{a^2 - (c^2 + b^2)}{-2bc}\right)} \tag{3}$$

where, r is the instantaneous projected distance of the screw force along screw length c, about the joint pivot defined at angle θ.

The overall gear ratio is nominally $52:1 \pm 3.5$ during level ground walking. At high flexion the gear ratio can sweep as low as $2:1$ as the actuator approaches limits to its controlled range of motion. Fig. 4 shows the change in r and overall gear ratio throughout the range of motion of the actuator. An alternative output arm is used in the knee configuration in order to bias the joint range of motion to remain fully controllable. The total range of controllable motion is 110 degrees. Mechanically, the system can reach 120 degrees to enable the additional range of motion for passive tasks such as when used as a knee actuator and a user wishes to sit cross-legged. Fig. 5(a,b) shows the actuator configuration, (c) shows the range of motion of the actuator as an ankle. The

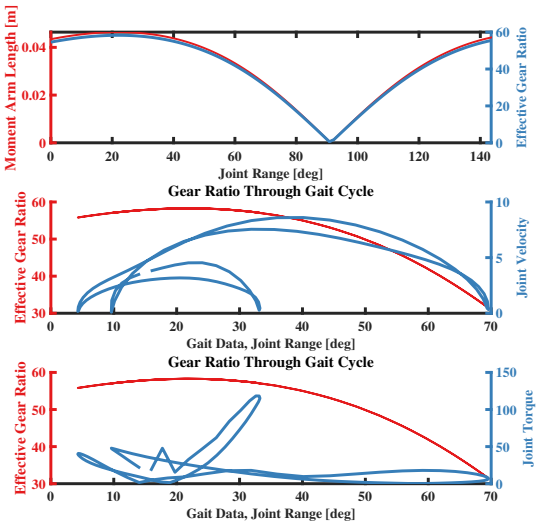

Fig. 4. The moment-arm changes throughout the range of motion of the output for the knee actuator. The top plot shows a singularity that is never reached due to joint offset that biases the joint back within range limits. The middle and bottom plots illustrate how the design optimization places the maximum moment-arm distance at the required power stroke of the knee as well as allocating a lower effective gear ratio within the range of higher velocity.

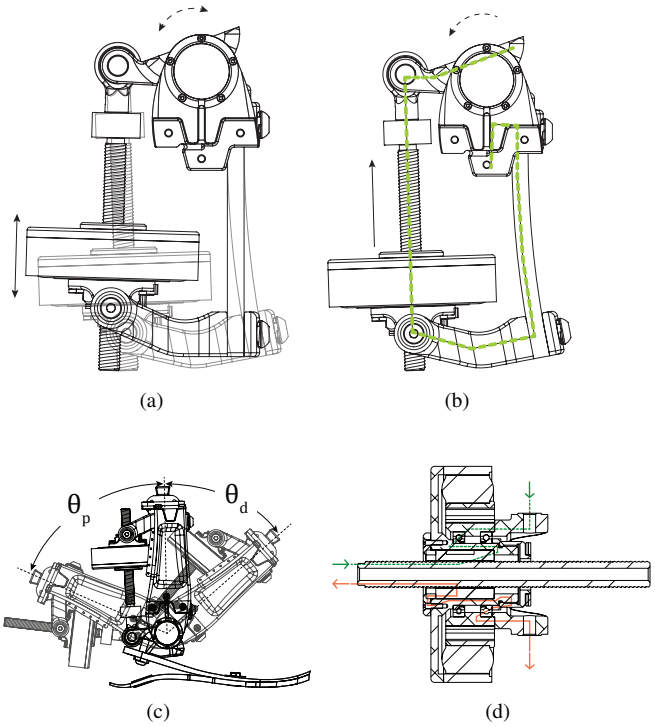

Fig. 5. (a) Spring deflection occurs when a torsional load (dotted arrow) is applied at the rotary output, reaction force from the motor/screw causes deflection of the spring. (b) Shows the load path from the applied load at the joint, through the linear actuator, the cantilever spring and to the structural frame. (c) The full range of motion of the ankle configured TF8 prosthesis. Motion is labeled as θ_d is dorsiflexion, and θ_p is plantarflexion. (d) Close-up of the ball-screw integrated into the motor. The compression load-path is shown as the dotted line, while the tension load-path is shown as the solid line through the motor bearing stack.

linear motion is achieved with a Thomson Linear 5mm lead ball-screw (BSPRM012L05M) and nut (KGM-N-1205-RH). The ball-nut is mounted directly in the rotor of a customized motor.

Though not tested in these experiments the rotor is designed to accommodate two other lead ball-screws: a 2mm and a 10mm lead. The 5mm lead screw is chosen for these experiments due to its ability to perform as both a knee and an ankle. Optimal performance for each joint can be achieved by swapping the appropriate ball-screw and nut into the respective joint actuator.

2) Motor: The motor is a high pole-count frameless motor built into a custom rotor and stator, based on the T-Motor U10 Plus KV100 outrunner motor [27]. The rotor is designed to house the ball-nut directly inside the motor, without the need or external couplings. Thin-section, angular contact bearings support the rotor and the high axial load imparted from the ball-screw. Axial pre-load of the bearings is generated by a retaining nut that also supports a magnetic motor encoder rotor disk. The motor bearing stack with ball-nut and its associated load path can be seen in Fig. 5(d). Due to the nature of the bearings ,compressive and tensile load paths differ and are shown in dotted and solid lines, respectively. The motor stator is mounted to the actuator spring frame by polymer bushings, while the pivot-rod end of the screw mounts to the output arm by way of a single needle bearing.

The motor choice is based on the performance of the motor when simulated as a complete actuator clamped to the specified output trajectory. Fig. 6 shows the expected motor torque speed and power speed trajectory when applied to an (a) ankle and (b) knee for a 90kg person walking at a nominal 1.25m/s. The nominal motor limits are shown as dotted lines and the absolute peak capacity are shown in solid lines. Due to the ”peaky” nature of walking we choose an actuator and motor combination that can achieve nearly all required waypoints, allowing trajectories outside of the nominal limits, but within the maximum current limited peak torques. To note there is velocity saturation expected for 3% of knee waypoints, yet headroom for torque capacity. These motor capacity plots show that the 5mm lead chosen is a compromise between ankle and knee trajectories; more ideally tuned combinations to maximize motor capacity would be a lower lead screw for the ankle, and higher lead screw for the knee.

3) Structure: The architecture of TF8 is defined as a moment-coupled, cantilever-beam, reaction-force series elastic actuator (MC-RFSEA). The reaction-force from the linear actuator induces a moment on a cantilever-beam spring by way of the motor stator being pinned to a moment arm that is clamped to the spring, thus creating a moment inducing force-couple. The spring serially grounds the output load to the frame of the actuator. Four bolts attach the spring, enabling its quick replacement to tune the performance of the actuator for a given application: such as users of different mass, to match the dynamics of either an ankle or knee, or enabling the equivalent of a sport or economy mode of operation for the actuator.

In this RFSEA configuration the actuator unloaded and high-impedance behavior differ from a traditional SEA. The

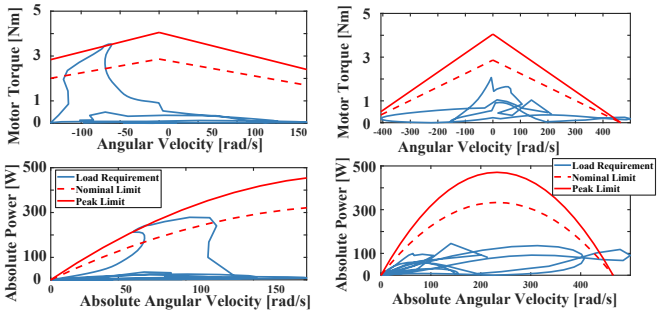

Fig. 6. These plots are the (a) ankle and (b) knee motor trajectories and limits of a 90 kg person walking at 2.0 m/s with as designed and optimal gear ratio. Using a screw lead of 0.005 mm for a nominal gear reduction of N=52.8. Solid line is motor peak limit, dotted line is nominal continuous limit. The knee actuator would benefit from a lower reduction ratio to better utilize the torque and velocity capability of the motor.

primary difference is the spring is serially located in the ground-path of the motor, rather than the output path of the actuator. The lumped parameter assumption commonly used for a SEA is not valid for free-space motions. In the high-impedance case motor-mass is also sprung with the rotor inertia. The performance of the high-impedance condition differs from the low-impedance moving-output condition by enabling an impulse load to deflect the spring and motor without rotating the motor inertia, thus improving high-frequency inertial conditions [28], [29].

The spring deflection during loading of the actuator is shown in Fig. 5(a,b). The dotted-line arrow represents an applied joint torque, τ_l and the solid arrow is force from motor displacement along the length of the screw, F_s. The green dotted line in Fig. 5(b) shows the load path when the structure experiences an internal compressive load that would be due to an ankle dorsiflexion or knee extension maneuver. The displacement shown is the maximum allowed deflection, limited by hard-stops built into the actuator structure (not shown). The configuration shown is the minimum viable actuator; the three staggered holes near the output pivot are mounting holes where the frame could be grounded to a support structure. In the application of a prosthesis the structure is swept back around the spring and motor in order to mount the device to a pyramid adapter. This structural routing could be designed for alternative applications.

4) Elastic Elements: The cyclical motion of gait is well suited to leverage the energy storage and power delivery capacity of springs [30]. The goal of the series elastic element design is to maximize energy storage (low stiffness) in the spring while also maximizing system control bandwidth (high stiffness) – two opposing objectives. Increasing spring stiffness improves natural frequency, but reduces the amount of energy that can be stored for a given loading condition, and puts greater precision requirements on encoder based force sensing. Reduced spring stiffness improves energy storage but also requires the motor to travel greater distance to reverse direction at high load.

The strain energy density and loading configuration determine the total energy storage capacity of a spring. The configuration of the series elastic element in TF8 is chosen for its bending dominated strain. In addition to the flat plate spring being simple to manufacture and affix, in pure bending it also exploits the material properties of composites. By aligning all tension and compressive forces with a unidirectional tensile fiber orientation, we fully leverage the asymmetric properties of composites. Thus, though the total strain in the beam includes bending, axial strains, and shear strains, it is heavily dominated by bending and axial forces:

$$U_{bend} = \frac{M^2 L}{2EI} = \frac{L(P_x t + L P_y)^2}{2EI} \tag{4}$$

$$U_{axial} = \frac{P_x^2 L}{2AE} \tag{5}$$

$$U_{shear} = \frac{P_y^2 h}{2AG} \tag{6}$$

$$U_{total} = U_{bend} + U_{axial} + U_{shear} \tag{7}$$

where, P_x, P_y are the longitudinal and transverse to the spring components of screw force F_s, defined as: $P_x = F_s \cos\theta_p$, $P_y = F_s \sin\theta_p$, and $\theta_p = \frac{F_s}{K_x t}$. K_s is linear spring stiffness, and t is the moment arm length as described in Fig. 3.

To define the spring geometry we numerically solve for the length, height and width of the spring, subject to a minimum mass objective, geometric constrains, and selected material properties. The target design parameters are specified from the initial clamped optimizations: stiffness K_s, and stored energy (7). The beam height is then solved from:

$$h = \sqrt{6\frac{(P_x t + P_y L)}{b \cdot \sigma_f}} \tag{8}$$

where, b and L are beam width and length, respectively, and σ_f is the allowable fatigue limit of the material. Similar to

The results of optimization defined a nominal series stiffness $K_s = 271\frac{kNm}{m}$, and an 8.6mm thick unidirectional fiberglass spring. Carbon fiber is of course optimal, but for cost reasons we went with a unidirectional E-glass fiberglass composite (GC-67-UCB) manufactured by Gordon Composites [31]; future iterations could benefit from a thinner carbon fiber beam. After initial testing we adjusted to a thicker spring to compensate for an overall lower than expected structural stiffness. The configuration as built has a 42 mm x 12.44 mm thickness beam with a sprung length of 86 mm and an overall measured linear stiffness of 378 kN/m. The maximum deflection is limited by mechanical features built into the structure; at the maximum 13mm of deflection the spring experiences nearly 265Nm or torque and stores 19 Joules of mechanical energy.

5) Mass and Height: The minimum working actuator configuration as shown in Fig. 5(a) has a mass of 1.3kg. The overall hardware mass as a knee, not including electronics or battery, measures 1.6kg. The electronics and wiring harness weigh 53g and 52g, respectively. The fully equipped actuator configured as an ankle such as Fig. 7 with on-board electronics, flex-foot, adapters and battery together weigh 2.0kg. The mass breakdown is shown in Table II.

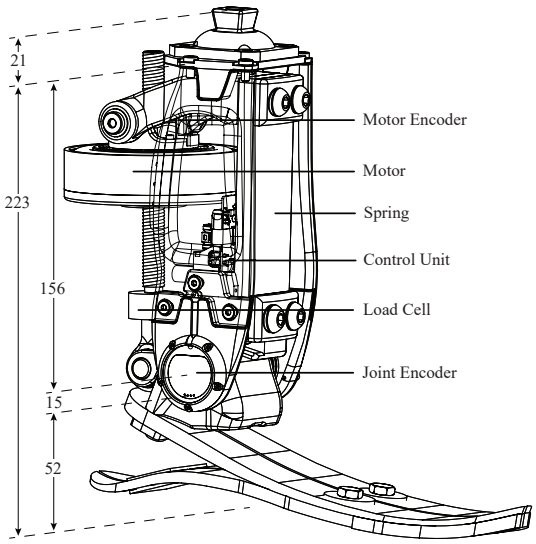

Fig. 7. The TF8 Actuator is shown configured as an ankle powered prosthesis with the main components labeled. The actuator minimum build height is 171mm measured between standardized mounting plates, shown here with standard prosthesis components attached. All dimensions are in millimeters.

TABLE II
MASS DISTRIBUTION OF THE TF8 KNEE ACTUATOR HARDWARE

Component	Mass (g)	(%)
Structural Components	556	35
Motor	549	34
Spring	116	7
Ballscrew	100	6
Spring Clamping Hardware	95	6
Load Cell	54	3
Electronics	53	3
Fasteners	48	3
Encoder Hardware	45	2
Total	**1616**	**100**

Configured as an ankle the output joint placement is designed to match the relative orientation of the BiOM [1] when mounted on an Össur Vari-flex foot [32] – the unloaded height of the ankle is 67mm and lateral placement with respect to mounting holes in the Vari-flex is matched. Matching alignment allows direct kinematic comparisons to BiOM/EmPower. When configured as an ankle the mounting height of a pyramid adapter is at an unloaded height of 223mm with a mass of 2.0kg, and as an ankle + knee the minimum height, without medial-lateral offset is 443mm, with a total mass of of 3.7kg.

6) Mechatronics: The mechatronic system is composed of a control unit that houses a mid-level controller, motor driver, battery management system, sensor inputs and communications to external peripherals. The control unit is a modified version of the Dephy Inc. FlexSEA system [33]. The mid-level controller is based on a STM32F427 180Mhz microprocessor. The block diagram of this control unit is shown in Fig. 8. The main loop in the control unit is operating at 1kHz, providing sensor updates, safety checks and controls, while the underlying motor drive current controller is operating at 20kHz. The external sensors include an absolute on-axis

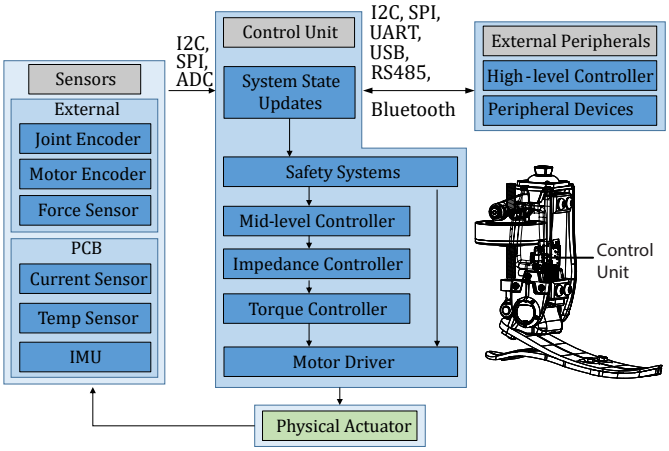

Fig. 8. The TF8 embedded system layout is shown in schematic form. The Control Unit is based on the FlexSEA embedded system developed by Dephy, Inc. consisting of a motor driver and a STM32F427 microcontroller. The system supports external peripheral devices, sensors, and common communication protocols.

joint encoder (AS5048B), incremental off-axis motor encoder, and load-cell (Futek LCM300). The load cell signal has a nine sample median filter and a 30Hz low-pass butterworth filter applied to reduce noise. Internal sensors include an inertial measurement unit, motor phase current sensor, wheatstone bridge strain-gauge circuit, and a temperature sensor. The peripheral communications allow communication between a host computer through USB, Bluetooth and RS485 for connection to additional FlexSEA units. An I^2C bus is used to communicate with an external electromyography (EMG) amplifier board also designed by our research group [34]. The battery used for walking experiments is composed of two 3S 11.1V 1.0Ah lithium polymer hobby-grade batteries connected in series for a nominal operating voltage of 22.2V and a lifetime of roughly 5500 steps; the battery combined mass is 180g and is usually strapped onto the socket of a test subject to reduce distal mass.

7) Control: The torque compensator is a proportional integral differential (PID) controller with integral anti-windup and a feed-forward term. A second order low-pass butterworth filter set at 20Hz cutoff frequency adjusts the torque reference to phase align with the feedback term. The feed-forward term is a notch filter defined by the inverted plant model estimated from the system identification, and made realizable with a 30Hz low-pass butterworth filter applied to the reference torque. The notch filter helps reduce excitation around the natural frequency of the RFSEA [28]. The PID controller gain tuning is done manually with the joint output rotor statically locked in position and 50Nm step impulses applied.

III. METHODS

A. System Characterization

To verify actuator load capabilities, and perform system identification we use the high-impedance, locked-output test method [35]. The locked-rotor experiments pushed the actuator to its designed fatigue-limit load rating of $175\mathrm{Nm}$ and to the maximum allowable spring deflection and hard-stop

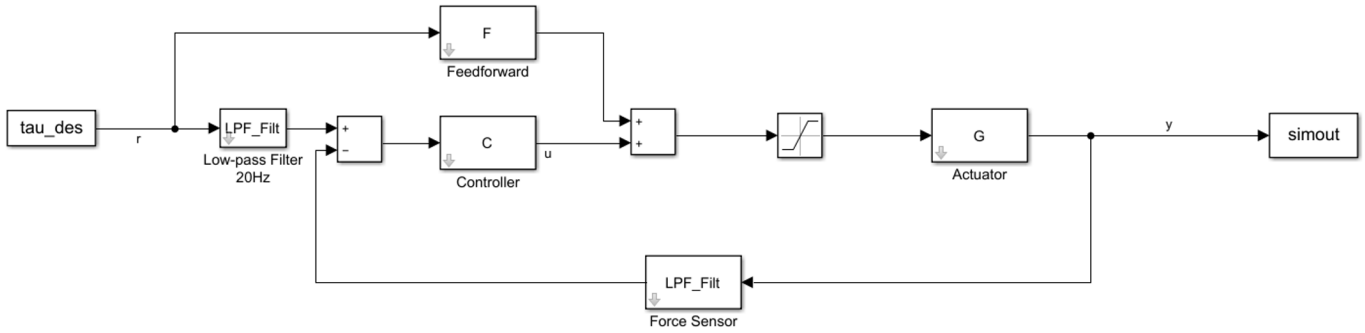

Fig. 9. Feedforward model based control block diagram. The low-pass filter is implemented within the feedforward term to make it realizable.

limited torque of $218\mathrm{Nm}$. To identify system characteristics of both the open-loop and closed-loop conditions of the locked rotor state we command a linear-ramping, sinusoidal chirp command of $\pm$50Nm torque amplitude, with 2.5Nm Gaussian white noise across the frequency range of 0.1-12Hz. Equivalent mass, stiffness and damping characteristics are then extracted from these models and used in control simulations to further tune the torque compensator.

1) Preliminary Clinical Evaluation: Subject testing was performed at the Massachusetts Institute of Technology (MIT) Media Lab Biomechatronics Gait Laboratory. Participants were informed of and consented to test protocols approved by the MIT Institutional Review Board: the Committee on the Use of Humans as Experimental Subjects. All subjects self-reported to be healthy with activity levels equivalent to K3 or above: having ambulatory activity with variable cadence.

To verify the ability of the actuator to replicate biologically relevant torque and velocity capabilities we test the actuator configured as a foot-ankle powered prosthesis, worn by human subjects with below knee amputation. The preliminary testing includes a 75kg male subject, with unilateral below knee amputation walking on a treadmill at specified speeds. Additionally, an initial experiment with an above knee subject was performed but no data is presented at this time. Experimental procedures include donning and adjustment of the TF8 to match the alignment and comfort of the participant's standard issued prosthesis.

The walking controller we implemented is a finite-state machine walking controller following similar methods to [36]–[39]. The state transitions are shown in Fig. 10. Joint torque is specified by the mid-level impedance controller. The impedance torque command follows the standard single-joint form: $\tau_d = K_d(\theta_{des} - \theta_l) - B(\dot{\theta}_l)$ where, τ_d is desired joint torque specified to the torque controller, θ_{des} is desired joint angle set point, θ_l is measured joint angle, and $\dot{\theta}_l$ is measured joint velocity. The initial impedance parameters were based on parameters in [40]. Control parameters were then tuned to match the comfort level of the subject as they acclimated to walking at self-selected speed with the powered ankle-foot system.

Stance is triggered by a heel-strike transition from swing, identified by an absolute torque signal greater than a defined threshold. During controlled-dorsiflexion a virtual unidirectional parallel spring is superposed onto the stance impedance settings. As the subject leans into the virtual parallel spring, joint torque rises until reaching a specified threshold at which point the powered plantarflexion state triggers. The joint angle set-point then ramps to a plantarflexed position along with a transition in virtual stiffness and damping. As the user is propelled forward and lifts their foot the measured torque drops below a threshold and the swing phase is triggered. Swing phase then rapidly moves the toe position into a dorsiflexed state to provide toe-clearance throughout swing. The controller then waits for the next heel strike.

The parameters available to tune include virtual parallel stiffness, push-off torque threshold, push-off torque ramp rate, push-off stiffness, toe-off angle and damping. During the experiments, on-board sensors recorded and transmitted, at a rate of 100Hz, the full actuator state across a wireless bluetooth communication protocol to a secondary computer. Data collected included joint angle, velocity, torque, finite-state, as well as motor current and voltage.

IV. Results

A. Control

Bode plots of both open and closed-loop system response in a high-impedance state are shown in Fig. 11. The open-loop frequency response aligns well with a second order mass spring damper system as characterized by:

$$G(s) = \frac{90}{s^2 + 20s + 120}. \tag{9}$$

The natural frequency is measured at about 1.5 Hz and calculated from the estimate in (9) at 1.6 Hz.

The torque controller is manually tuned to achieve an under-damped response with relatively quick rise-time. The response to a 50Nm step-input applied to the locked-rotor configuration is shown in Fig. 12. The rise time T_r = 0.072 s, peak time T_p = 0.096s, with a percent overshoot of OS = 20%, and settling time of T_s = 0.232s. This results in a system estimate of closed-loop natural frequency $\omega_n = 5.9$ Hz, and damping ratio ζ = 0.47.

The closed-loop frequency response aligns well with a second order mass spring damper system as characterized by:

$$G(s) = \frac{920}{s^2 + 30s + 980}. \tag{10}$$

The natural frequency is 3.9Hz. The closed-loop -3dB bandwidth is 6.2Hz with a phase margin of 61.5 degrees.

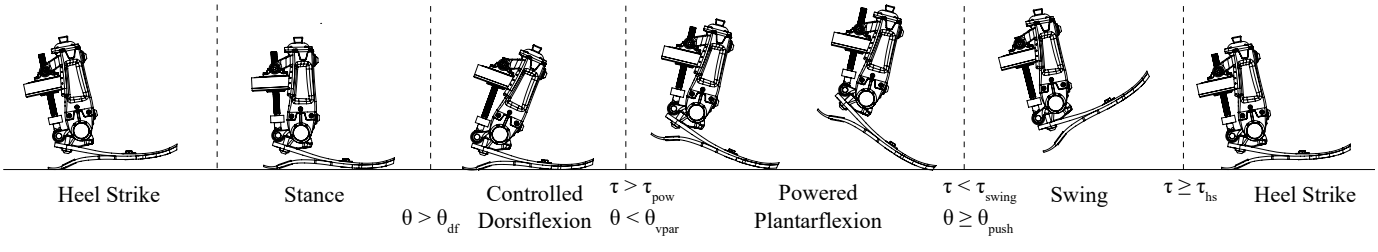

(a)

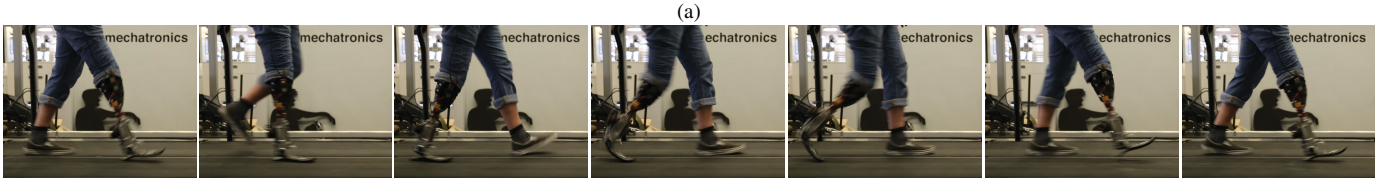

(b)

Fig. 10. Schematic and human subject demonstration of state transitions: (a) State transitions are triggered by torque and angle thresholds tuned to meet test subject preferences. (b) A subject walking with the finite-state machine controller. Note during powered plantarflexion the additional series elasticity contributed by the Variflex foot that is not accounted for in the numerical models.

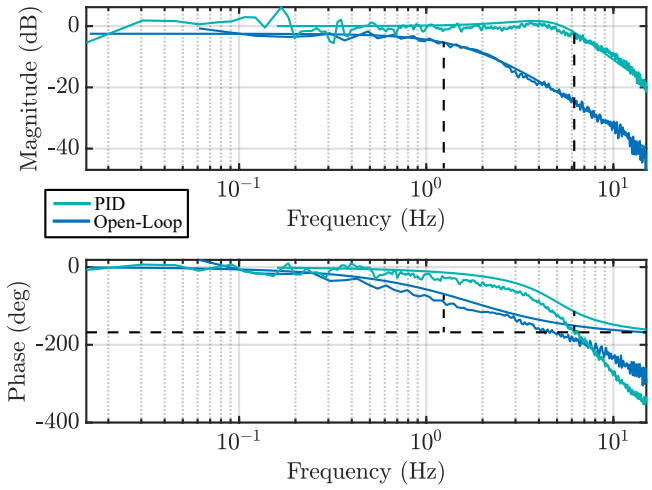

Fig. 11. Open-loop frequency response shows a damped second order system with natural frequency at 1.5 Hz and phase margin of -80^o. Closed-loop (PID) frequency response shows a damped second order system with natural frequency at 3.9 Hz, control bandwidth at 6.2 Hz, and phase margin of 61.5 degrees. The solid line is the estimated system response.

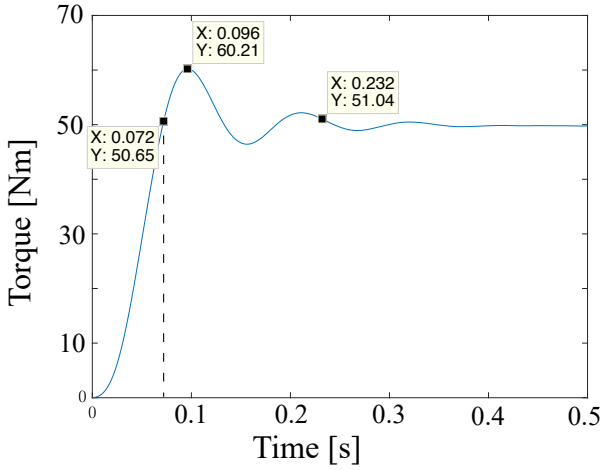

Fig. 12. A 50Nm step-response of the closed-loop torque controller collected with the actuator in a fixed-output (high-impedance) condition.

B. Preliminary Clinical Evaluation

Torque and power from a 75kg participant with unilateral below knee amputation walking with a finite-state machine controller on a treadmill at 1.5 m/s is shown in Fig. 13. Twenty-eight strides were acquired and normalized to percent gait cycle. The coefficient of determination between the biological mean and powered prosthesis mean data is $R^2 = 0.85$ for joint torque and $R^2 = 0.90$ for mechanical power. Joint torque is shown to reach 110Nm and joint power reaches 300W in these walking experiments.

The net positive, mean mechanical energy produced by the actuator over the 28 strides is 12 Joules. The mean electrical energy consumption by the actuator is $28 \pm 4J$. Fig. 14(a) compares biological mechanical energy to that measured on the prosthesis. In Fig. 14(b) the cumulative electric energy per stride is shown, comparing the simulated expectation of the actuator and that measured at the motor driver of the TF8 system.

V. Discussion

The mechanical design of the TF8 MC-RFSEA creates a low part-count, and mass efficient mechanical package. The moment-couple produces uniform strain along the length of the elastic cantilever-beam, maximizing utilization of asymmetric composite material layups, and thus maximizing strain energy density. Manufacturing the flat plate cantilever beam is relatively straightforward, enabling multitudes of springs to be available to tune performance to different users or applications. The TF8 design enables static reconfiguration: by releasing four bolts the spring can be swapped for a another to match user mass and application. This functionality is similar to [41] but with a simpler attachment means without adjusting the cantilever length. This spring arrangement also allows a build height reduction by wrapping the spring back along the

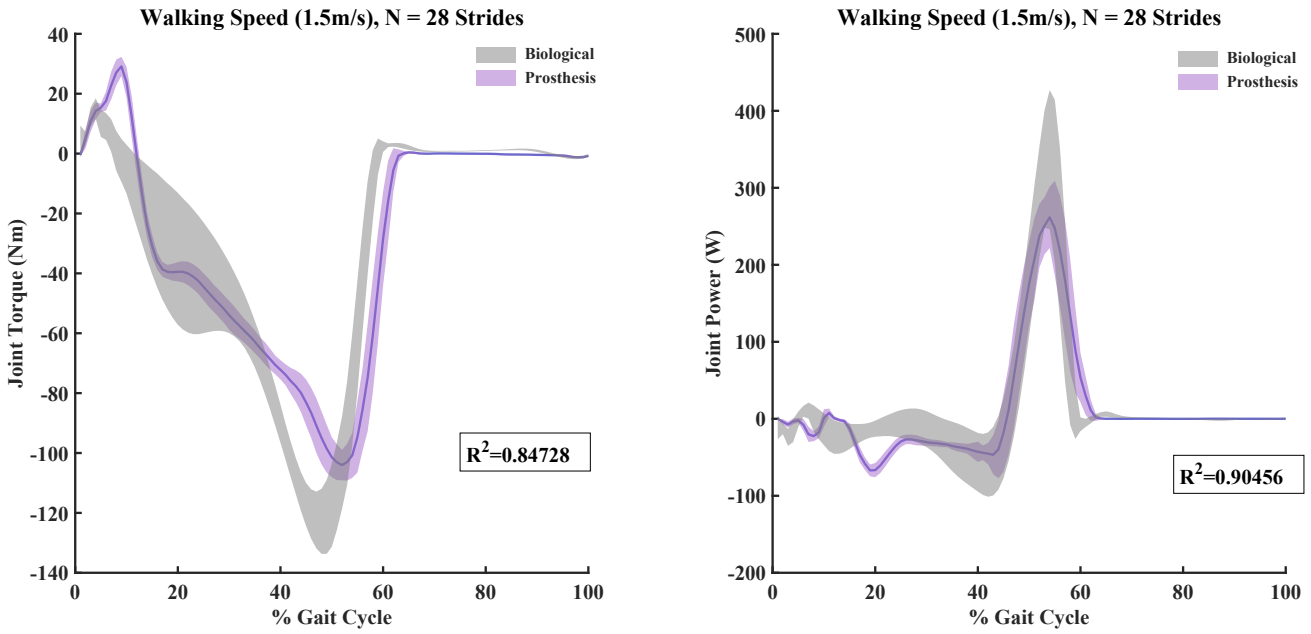

Fig. 13. Preliminary results from two subjects walking with the finite state-machine controller. Subject one data (a-b) is treadmill walking at 1.5m/s. The purple regions are one standard deviation of data collected on the TF8 prosthesis, the black line is the mean. Grey is one standard deviation of able-bodied walking data from [19].

length of the linear actuator, rather than a traditional SEA arrangement of coil springs stacked serially along the linear actuator axis that also rely on secondary linear bearings to support motion of the intermediary coupling between spring, motor and output [42]. In this case, the spring acts as a flexure to support lateral displacements of both the spring and motor. This design improves upon the leaf-spring configuration [43] used, by replacing the universal joint constraints with spring flexure constraints. Combining a ball-nut with an outrunner motor rotor and the use of a yoke pivot is similar to [25] but rather than serially stacked discrete components, our new design integrates the nut directly into the rotor and the supporting yoke directly into the stator support. These system integrations allow the ball-screw to pass entirely through the motor, increasing range of motion while decreasing build height, reducing part-count, complexity and mass.

The relatively high-torque of the U10Plus motor allows a smaller gear reduction than the smaller diameter Maxon EC-4 Pole inner rotor motor commonly used in other published hardware [9], [36], [44]. Reflected inertia is a critical parameter in both control bandwidth as well as user safety in high impedance contact conditions. Larger radius motors have an r^2 inertia increase yet are not subject to as large of a N^2 drivetrain reflected inertia contribution. Though the trade-offs between reflected inertia of rotor and drivetrain tends to nullify one another [45], reduced gearing generally benefits drivetrain efficiency; higher torque motors with lower drivetrain reduction ratios tend to have slightly improved performance.

A secondary user experience driver towards larger torque motors is that smaller diameter motors operate at higher rpm, generating higher frequency audible noise. Removing this high frequency element can reduce the audible noise range to a more qualitatively pleasing frequency range.

The larger inertia of the outrunner motor does, however, have a drawback related to its larger inertia. The reaction torque from high motor accelerations can propagate through the structural chain causing a twisting moment at the socket interface to the test subject. This motor can generate up to 3.5Nm of torque in normal operation, and while that reaction torque was initially considered in the loading on the spring, its effect on the wearer was not realized until parts were already under manufacture. The solution to this problem is smooth minimum jerk trajectory generation to minimize the reaction yaw torque on the user.

There are three conditions that occur with the load path configuration of this actuator that could be improved: the first is inherent to the sprung mass of the reaction-force configuration, the second is overall structural stiffness, and the third is small transverse backlash around zero-load. These last two issues could be mitigated with a second design iteration. The actuator remains fully controllable even with these design flaws however they do show up as small non-linearities in operation. The reaction-force spring configuration creates a relatively large sprung mass of the motor, moment arm and spring. The motion trace image in Fig. 5(a) demonstrates the sprung behavior of the motor mass. System stiffness is limited by the bolted interface that routes the ground path past the spring to the pyramid adapter. A single monolithic structure

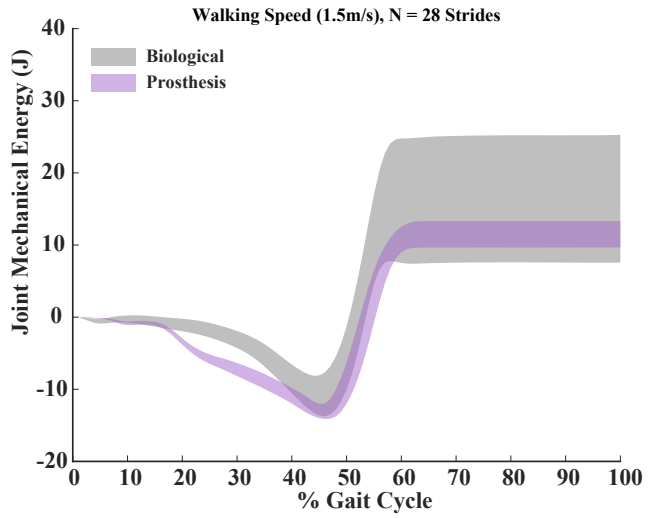

(a)

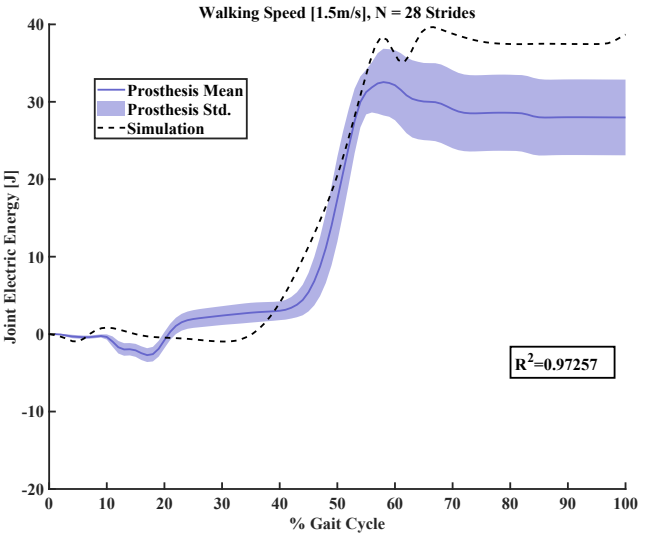

(b)

Fig. 14. Preliminary results from two subjects walking with the finite state-machine controller. Subject one data (a) is treadmill walking at 1.5m/s. Mechanical energy output at the joint shows alignment within one standard deviation of the biological dataset for 1.5 m/s walking. (b) Cumulative electric energy consumption by the robot during the 1.5m/s walking trials. Dotted line is simulated energy consumption, shaded is mean and one standard deviation from 28 strides. The mean overall electric COT is 0.053 with a cumulative energy of $28 \pm 4J$.

would reduce the compliance in the bolted joints. The center of the ball-nut is located offset from the motor support pivot, leading to a slight over-center condition near zero-load during compressive loading of the screw. Once loaded the ball-nut preloads in one direction or another. This design issues has not proven a problem in testing on the bench or with human participants, however it may lead to premature failure of the ball-nut.

The controllable torque bandwidth of the TF8 system while adequate at 6.2Hz is lower than expected. The additional reflected sprung mass of the motor in addition to rotor inertia during high impedance motions reduces system natural frequency. This increases the need for clean force signals and accurate current control in order to push the closed-loop controlled bandwidth beyond the natural resonant frequency that lies within the expected operating range. Similarly disappointing is the level of overshoot in step response. The calculated power output of the actuator should be more than 1kW mechanical power, however, in the experiments shown here 300W is the maximum achieved. Controllability at higher powers seems to be highly dependent on power supply. It turns out the motor torque is saturating due to a mismatch in motor impedance and driver switching frequency causing ineffective motor commutation. Current is being sunk into the motor windings, and tuning the current controller shows accurate current tracking, but it is not effectively generating torque. After extensive testing we found the motor inductance is 5.5 times lower than originally specified; the motor inductance of 30.3μH is much too low for the 20kHz switching frequency of the motor driver. Our motor simulations expected to reach 175Nm torques with 35A of motor current, however in practice 60A is required to achieve these torque levels, maxing out our driver capability.

The motor phase current saturates due to the relatively long switching period, causing current ripple in the phase windings. The current controller is operating correctly, but the current is not generating torque effectively. To understand how inductance affects the current ripple for a motor, the current ripple on a buck converter can be used as a tool [46]. The original motor specification claimed to have 0.168mH and so a switching frequency of 20kHz would have resulted in a ripple current of 6.5A and 2.5W power loss, assuming a 50% duty cycle. However, with the actual motor inductance being 0.03mH, this current ripple reaches 35A and over 75W of power loss in the windings! At higher duty cycle this gets worse, and explains why torque saturation was observed at outputs above 110Nm at the joint. This mismatch in switching frequency makes it difficult to achieve a critically damped step response even with more sophisticated model-based control methods. Despite dumping current into the motor coils, if it is not timed correctly, it is not possible to generate useful torque at the rotor. This torque lag limits the ability to apply and re-direct motor torque, limiting controllability of the actuator at higher loads. Future improvements would be to increase motor inductance, at the cost of increased winding resistance in order to better match the switching frequency of the motor driver. One efficiency balance that needs to be estimated is the trade-off in increasing winding resistance compared to increasing switching frequency which causes switching losses at the driver switches.

Walking with a finite-state machine shows the actuator generally tracks biological kinetics and kinematics but has room for improvement. The actuator is shown capable of achieving biological torque and power within an $R^2 \geq 0.85$ and $R^2 \geq 0.85$. The ankle joint mean torque shows a slight phase-lag and undershoot of mean data, though does achieve about 108Nm at powered push-off. Mechanical power aligns well with mean data, but again the mean 250W measured at the joint undershoots biological mean power of 380W, for a 75kg subject. The mismatch between motor and driver means the maximum velocity and power of the actuator could not be

fully evaluated at this time. Based on all other metrics tracking close to the simulated behavior we feel safe to estimate the maximum velocity of the output with the 5mm lead screw should achieve 6.8rad/s, and with the knee optimal 10mm screw a 13rad/s output should be realizable.

The measured energetics at the 1.5m/s walking speed do align well with the simulations. Mechanical energy of 12J was generated at the joint, and that matches within one standard deviation of the biological data set. The electric energy consumption of the actuator measured below the expected 38J at $28 \pm 4J$. Nonetheless, the TF8 does produce 0.16J/kg of positive net-work at the ankle, aligning within one standard deviation of biological walking energy.

The measured eCOT is rarely published but should be. It is a useful metric to compare overall system efficiency for mobile, wearable robots. The Au *et. al.* ankle has a eCOT of 0.06J at 1.25m/s walking speed. Our TF8 improves over that early ankle showing an eCOT = 0.053J/kg measured at 1.5m/s walking speed. This outperforms the Au ankle and matches closely the simulations shown in Fig. 2 tracking energy within $R^2 = 0.97$.

VI. Conclusions

The TF8 actuator is a light weight, powerful actuation platform, that shows promise of enabling high-activity-level performance as both knee and ankle bionic joints. We have shown it is capable of producing 175 Nm of torque, biological ranges of power and maintains a mass of 1.6-2.0 kg, making it one of the lighter weight and more powerful research-grade powered prostheses yet published. By integrating the ball-nut directly into the motor rotor and utilizing the spring as both energy storage and motion constraint we are able to reduce the design complexity and build the actuator into a standalone actuation unit. These design choices both improve maintenance requirements and overall system costs. Further, the TF8 actuator could potentially be used for other humanoid, quadruped or robotic applications by replacing the structural elements with other application specific hardware and springs.

The optimization method of searching for a minimum eCOT design specification proved effective, though the physical limits of discrete components limits the ability to smoothly search across the design space and thus enforces compromise in the design. The kinematically clamped optimization is a good starting point for design, however the constraints used in this analysis are overly strict. A more sophisticated actuator model that includes motor/drive effects and controller effort and a linear regression error tracking would broaden the design space and possibly provide for better overall trajectory tracking and final system response.

Finally, in the design of TF8 we attempted to not only build a high performance, cost-effective actuator capable of performing multiple functionalities, we also strove to include aesthetic in the design of our hardware. At the end of the day we are building hardware to replace the function of lost body-parts. The people who have the opportunity to make use of our hardware should be inspired not only by the technology but by our effort to push the limits of how disability is perceived.

Acknowledgment

The authors would like to thank our brave test-pilots and the machine shops who helped produce great hardware, and in particular the MIT Central Machine Shop, and Mark Belanger at MIT Edgerton Student Shop. Finally, the authors thank our funding sources for enabling this research, and our colleagues in the field contributing to the greater knowledge.

References

[1] Bionx, "The BiOM Advantage - BionX Medical Technologies," 2017.
[2] Össur, "Össur Dynamic Solutions Power Knee™," 2018.
[3] G. Pratt, M. M. Williamson, and Others, "Series elastic actuators," vol. 1. IEEE, 1995, pp. 399–406.
[4] S. K. Au, J. Weber, and H. Herr, "Biomechanical Design of a Powered Ankle-Foot Prosthesis," in *IEEE 10th International Conference on Rehabilitation Robotics*, 2007, pp. 298–303.
[5] P. Cherelle, V. Grosu, A. Matthys, B. Vanderborght, and D. Lefeber, "Design and validation of the ankle mimicking prosthetic (AMP-) Foot 2.0," *IEEE Transactions on Neural Systems and Rehabilitation Engineering*, vol. 22, no. 1, pp. 138–148, 2014.
[6] P. Cherelle, V. Grosu, M. Cestari, B. Vanderborght, and D. Lefeber, "The AMP-Foot 3, new generation propulsive prosthetic feet with explosive motion characteristics: Design and validation," *BioMedical Engineering Online*, vol. 15, no. 3, pp. 21–36, 2016.
[7] R. D. Bellman, M. A. Holgate, and T. G. Sugar, "SPARKy 3: Design of an active robotic ankle prosthesis with two actuated degrees of freedom using regenerative kinetics," *Proceedings of the 2nd Biennial IEEE/RAS-EMBS International Conference on Biomedical Robotics and Biomechatronics, BioRob 2008*, pp. 511–516, 2008.
[8] M. A. Holgate, J. K. Hitt, R. D. Bellman, T. G. Sugar, and K. W. Hollander, "The SPARKy (spring ankle with regenerative kinetics) project: Choosing a DC motor based actuation method," *Proceedings of the 2nd Biennial IEEE/RAS-EMBS International Conference on Biomedical Robotics and Biomechatronics, BioRob 2008*, pp. 163–168, 2008.
[9] M. Grimmer, M. Holgate, J. Ward, and A. Boehler, "Feasibility study of transtibial amputee walking using a powered prosthetic foot," in *International Conference on Rehabilitation Robotics (ICORR)*, 2017, pp. 1118–1123.
[10] Ottobock, "C-Leg 4: Microprocessor Knee — Ottobock UK," 2018.
[11] A. D. Kuo, "A simple model of bipedal walking predicts the preferred speed-step length relationship." *Journal of biomechanical engineering*, vol. 123, no. 3, pp. 264–269, 2001.
[12] A. Protopapadaki, W. I. Drechsler, M. C. Cramp, F. J. Coutts, and O. M. Scott, "Hip, knee, ankle kinematics and kinetics during stair ascent and descent in healthy young individuals," *Clinical Biomechanics*, vol. 22, no. 2, pp. 203–210, 2007.
[13] B. E. Lawson, H. A. Varol, A. Huff, E. Erdemir, and M. Goldfarb, "Control of stair ascent and descent with a powered transfemoral prosthesis," *IEEE Transactions on Neural Systems and Rehabilitation Engineering*, vol. 21, no. 3, pp. 466–473, 2013.
[14] T. Lenzi, M. Cempini, L. J. Hargrove, and T. A. Kuiken, "Design, Development, and Testing of a Lightweight Hybrid Robotic Knee Prosthesis," *International Journal of Robotics Research*, vol. in press, 2018.
[15] E. J. Rouse, L. M. Mooney, E. C. Martinez-Villalpando, and H. M. Herr, "A Clutchable Series-Elastic Actuator: Design of a Robotic Knee Prosthesis for Minimum Energy Consumption," in *Proceedings of the IEEE International Conference on Rehabilitation Robotics*, 2013.
[16] E. C. Martinez-Villalpando, J. Weber, G. Elliott, and H. Herr, "Design of an Agonist-Antagonist Active Knee Prosthesis," in *International IEEE/EMBS Conference on Biomedical Robotics and Biomechatronics*. Scottsdale, AZ: IEEE, 2008.
[17] H. Zhao, E. Ambrose, and A. D. Ames, "Preliminary Results on Energy Efficient 3D Prosthetic Walking with a Powered Compliant Transfemoral Prosthesis," in *IEEE International Conference on Robotics and Automation (ICRA)*, Singapore, 2017, pp. 1140–1147.
[18] M. E. Carney and H. Herr, "Electric-Energetic Consequences of Springs in Lower-Extremity Powered Prostheses on Varied Terrain," *Proceedings of the IEEE RAS and EMBS International Conference on Biomedical Robotics and Biomechatronics*, vol. 2020-Novem, pp. 989–996, 2020.
[19] J. Markowitz, "A Data-Driven Neuromuscular Model of Walking and its Application to Prosthesis Control," Ph.D. dissertation, Massachusetts Institute of Technology, 2013.

[20] D. S. Pieringer, M. Grimmer, M. F. Russold, and R. Riener, "Review of the actuators of active knee prostheses and their target design outputs for activities of daily living," *2017 International Conference on Rehabilitation Robotics (ICORR)*, pp. 1246–1253, 2017.

[21] M. D. Grabiner, T. J. Koh, T. M. Lundin, and D. W. Jahnigen, "Kinematics of recovery from a stumble," *Journals of Gerontology*, vol. 48, no. 3, pp. 97–102, 1993.

[22] R. Drillis, R. Contini, and M. Bluestein, "Body Segment Parameters; a Survey of Measurement Techniques." *Artificial limbs*, vol. 25, pp. 44–66, 1964.

[23] C. E. Clauser, J. T. McConville, and J. W. Young, "Weight, Volume, and Center of Mass of Segments of the Human Body," *National Technical Information Service*, pp. 1–112, 1969.

[24] T. Verstraten *et al.*, "Optimizing the power and energy consumption of powered prosthetic ankles with series and parallel elasticity," *Mechanism and Machine Theory*, vol. 116, pp. 419–432, 2017.

[25] S. Wang, C. Meijneke, and H. van der Kooij, "Modeling, design, and optimization of Mindwalker series elastic joint," in *IEEE International Conference on Rehabilitation Robotics*, Seattle, WA, jun 2013, pp. 1–8.

[26] E. J. Rouse, L. M. Mooney, and H. M. Herr, "Clutchable series-elastic actuator: Implications for prosthetic knee design," *The International Journal of Robotics Research*, vol. 33, no. 13, pp. 1–15, nov 2014.

[27] T-Motor, "T-Motor," 2017.

[28] N. Paine, S. Oh, and L. Sentis, "Design and Control Considerations for High-Performance Series Elastic Actuators," *IEEE/ASME Transactions on Mechatronics*, vol. 19, no. 3, pp. 1080–1091, jun 2014.

[29] V. L. Orekhov, C. S. Knabe, M. A. Hopkins, and D. W. Hong, "An unlumped model for linear series elastic actuators with ball screw drives," in *International Conference on Intelligent Robots and Automation*. IEEE, 2015, pp. 2224–2230.

[30] D. Paluska and H. Herr, "The effect of series elasticity on actuator power and work output: Implications for robotic and prosthetic joint design," *Robotics and Autonomous Systems*, vol. 54, pp. 667–673, 2006.

[31] Gordon Composites, "GC-67-UB," Gordon Composites, Montrose, Colorado, Tech. Rep., 2017.

[32] Össur, "Vari-Flex," Össur, Tech. Rep., 2019.

[33] J. F. Duval and H. M. Herr, "FlexSEA: Flexible, Scalable Electronics Architecture for wearable robotic applications," *Proceedings of the IEEE RAS and EMBS International Conference on Biomedical Robotics and Biomechatronics*, vol. 2016-July, pp. 1236–1241, 2016.

[34] S. H. Yeon, "Design of an Advanced sEMG Processor for Wearable Robotics Applications," Ph.D. dissertation, Massachusetts Institute of Technology, 2019.

[35] D. W. Robinson, "Design and analysis of series elasticity in closed-loop actuator force control," Ph.D. dissertation, Massachusetts Institute of Technology, 2000.

[36] S. K. Au and H. M. Herr, "Powered Ankle-Foot Prosthesis," *IEEE Robotics & Automation Magazine*, no. September, pp. 52–59, 2008.

[37] M. Goldfarb *et al.*, "Realizing the promise of robotic leg prostheses." *Science translational medicine*, vol. 5, no. 210, p. 210ps15, nov 2013.

[38] B. E. Lawson *et al.*, "A robotic leg prosthesis: Design, control, and implementation," *IEEE Robotics and Automation Magazine*, vol. 21, no. 4, pp. 70–81, 2014.

[39] A. H. Shultz, B. E. Lawson, and M. Goldfarb, "Running with a powered knee and ankle prosthesis," *IEEE Transactions on Neural Systems and Rehabilitation Engineering*, vol. 23, no. 3, pp. 403–412, 2015.

[40] F. Sup, A. Bohara, and M. Goldfarb, "Design and Control of a Powered Knee and Ankle Prosthesis," in *IEEE 10th International Conference on Rehabilitation Robotics*. Noordwijk, The Netherlands: IEEE, 2007, pp. 4134–4139.

[41] V. Orekhov, D. Lahr, B. Lee, and D. Hong, "Configurable Compliance for Series Elastic Actuators," in *ASME 2013 IDETC/CIEC*. Portland, Oregon: ASME, 2013, pp. 1–8.

[42] D. W. Robinson, J. E. Pratt, D. J. Paluska, and G. A. Pratt, "Series elastic actuator development for a biomimetic walking robot," in *International Conference on Advanced Intelligent Mechatronics*. Atlanta: IEEE/ASME, 1999, pp. 561–568.

[43] C. Knabe, B. Lee, V. Orekhov, and D. Hong, "Design of a Compact, Lightweight, Electromechanical Linear Series Elastic Actuator," in *ASME. International Design Engineering Technical Conferences and Computers and Information in Engineering Conference, Volume 5B: 38th Mechanisms and Robotics Conference*. Buffalo, NY: ASME, 2014, pp. 1–8.

[44] J. Zhu, H. She, and Q. Huang, "PANTOE II: Improved Version of a Powered Transtibial Prosthesis With Ankle and Toe Joints," in *Proceedings of the 2018 Design of Medical Devices Conference*. Minneapolis, MN, USA: ASME, 2018, pp. 1–3.

[45] A. Wang, S. Seok, A. Wang, D. Otten, and S. Kim, "Actuator Design for High Force Proprioceptive Control in Fast Legged Locomotion Actuator Design for High Force Proprioceptive Control in Fast Legged Locomotion," in *IEEE/RSJ International Conference on Intelligent Robots and Systems*, no. October. Vilamoura: IEEE, 2012, pp. 1970–1975.

[46] L. M. Mooney, "Autonomous Powered Exoskeleton to Improve the Efficiency of Human Walking," Ph.D. dissertation, Massachusetts Institute of Technology, 2016.

Matthew Carney received his B.S. Mechanical Engineering from California Polytechnic State University (CalPoly SLO) in 2004, the M.S. Mechanical Engineering from UC Berkeley in 2008, a S.M. Media Arts and Sciences in 2015 and a Biomechatronics Ph.D. in 2020 from Massachusetts Institute of Technology. His interests include machine design, mechatronics, and building hardware that improves lives, at scale.

Tony Shu received the B.S. in Materials Science and Engineering ('16) with highest honors from the Georgia Institute of Technology. He is currently a graduate student within the Biomechatronics Group at the MIT Media Lab. His research focuses on developing biomechanical lower limb models and control methodologies for intuitive control of powered prostheses by persons with amputation.

Roman Stolyarov received his Bachelor's Degrees in biology, computer science, and mathematics from Southern Methodist University in Dallas, TX. He is currently pursuing his Ph.D. in Medical Engineering and Medical Physics at the Harvard/MIT Health Sciences and Technology Department, where he is developing methods to control powered lower limb prostheses. His interests include robotics, machine learning, and human-machine interfacing.

Jean-François Duval received a bachelor's degree in Electrical Engineering from Université de Sherbrooke (Sherbrooke, Québec, Canada) and a master's degree from the Massachusetts Institute of Technology (Cambridge, MA). He developed his embedded system and power electronics expertise working on humanoid robots and electric vehicles, both in academia and industry. He designed the FlexSEA embedded system as part of his graduate work at the MIT Biomechatronics research group.

Hugh Herr heads the Biomechatronics group at the MIT Media Lab. He is the author and co-author of more than 150 peer-reviewed papers spanning the fields of biomechanics, biological motion control, as well as the technological innovations of human rehabilitation and augmentation technologies. Herr's Biomechatronics group has developed gait-adaptive knee prostheses for transfemoral amputees and variable impedance ankle-foot orthoses, among other innovations.